ACS OMEGA

Article

Cite This: ACS Omega 2018, 3, 8963−8970

http://pubs.acs.org/journal/acsodf

Correlations between Reduction Degree and Catalytic Properties of WO_x Nanoparticles

Febrigia Ghana Rinaldi,[†] Osi Arutanti,[‡] Aditya Farhan Arif,[†] Tomoyuki Hirano,[†] Takashi Ogi,*[,†] and Kikuo Okuyama[†]

[†]Department of Chemical Engineering, Graduate School of Engineering, Hiroshima University, 1-4-1 Kagamiyama, Higashi Hiroshima 739-8527, Japan

[‡]Research Center for Chemistry, Indonesian Institute of Sciences, Kawasan Puspitek, Serpong, Tangerang 15314, Indonesia

Supporting Information

ABSTRACT: Degrading organic dyes via catalytic processes for waste water purification is an important research topic from the environmental conservation point of view. Herein, the catalytic performance of tungsten blue oxide (WO_x) nanoparticles was investigated systematically by varying the reduction temperature. The optimum reduction temperature to obtain the most stable WO_x phase was obtained when plasma-synthesized WO_3 nanoparticles were thermally reduced at 425 °C. The as-synthesized nanoparticles had an average diameter of 10 nm and a calculated band gap of 2.37 eV, which is lower than that of the WO_3 nanoparticles (2.61 eV). The WO_x nanoparticles exhibited an excellent performance in degrading rhodamine B under dark conditions and visible light irradiation, with a reaction rate constant 93 times higher than that of the WO_3 nanoparticles.

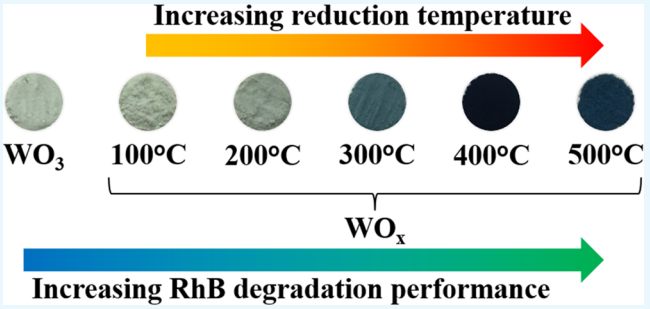

INTRODUCTION

In the past decade, tungsten oxide (WO_3) nanoparticles (NPs) have attracted much attention as an efficient material for photocatalysis, phototherapy, and electrochemical applications, due to their favorable physical and chemical properties.[1−4] Their relatively narrow band gap of 2.6−3.0 eV allows for excitation by visible wavelengths, which is desirable for photocatalysis applications.[5,6] The favorable surface interaction between tungsten oxide and organic dye molecules also makes it a good adsorbent.[7] The interaction between dye molecules and WO_3 nanosheet surfaces has been reported previously. WO_3 NPs in the form of films or nanosheets were used as adsorbents, and exhibited selective adsorption properties, though the amount of adsorbed material was not high.[8] Another report proposed the structuration of WO_3 NPs to enhance their surface area, which improved their adsorption properties and photocatalytic performance.[9,10]

A nonstoichiometric phase of WO_3 known as tungsten blue oxide (WO_x) NPs has recently received much interest. The presence of oxygen vacancies within its structure provides several advantages compared to WO_3.[11,12] For example, oxygen vacancies in the transition-metal oxide figuratively act as dopants, which decreases the band gap in a way similar to the addition of Pt onto TiO_x NPs.[13,14] Hence, an intrinsic semiconductor can be converted to a hypothetically extrinsic semiconductor with a donor activation energy at 0.01 eV.[11] WO_x NPs also have the ability to generate free electrons ($N \sim 10^{21}$ cm^{-3}).[12]

Numerous approaches have been developed for synthesis of WO_x NPs, including approaches based on supercritical fluid, sol gel, hydrothermal, and chemical vapor deposition methods.[15−17] WO_x particles can reportedly be produced by heating ammonium paratungstate $[(NH_4)_{10}(H_2W_{12}O_{42})\cdot 4H_2O]$ for several hours, which is feasible for industrial-scale applications.[18] The use of WO_x particles in various forms and morphologies, such as Ag/WO_x nanorods, WO_x−TiO_2 composites, WO_x/C nanocomposites, and WO_x nanorods, for photocatalytic application has been previously reported.[12,19−21] Such reports have shown that other than the presence of an additional dopant or cocatalyst, increasing the amount of oxygen vacancies inside the crystal structure could improve the photocatalytic performance. However, most resulting products were reportedly larger than 100 nm. Nanosized particles (i.e., smaller than 100 nm) are preferred because higher specific surface area gives them higher activity. To the best of our knowledge, there are still no reports on synthesis of WO_x NPs smaller than 100 nm via thermal reduction methods at reduction temperatures in the range of 300−700 °C. Furthermore, there are also no reports regarding the effect of reduction temperature on their catalytic performances under dark condition and light irradiation for organic dye degradation.

Received: May 24, 2018
Accepted: August 3, 2018
Published: August 13, 2018

DOI: 10.1021/acsomega.8b01110
ACS Omega 2018, 3, 8963−8970

In the current study, WO_x NPs were synthesized from plasma-synthesized WO_3 NPs (average diameter of 6 nm) via a thermal reduction process under 100% H_2 gas inside an electric furnace. The effect of the reduction temperature on the physicochemical properties of the resulting WO_x NPs, including size, specific surface area, and band gap value, was investigated systematically. The degradation of rhodamine B (RhB) under dark conditions and visible light irradiation was studied to evaluate the adsorption and photocatalytic performance of the as-synthesized WO_x NPs.

RESULTS AND DISCUSSION

Effect of Reduction Temperature. Figure 1 shows X-ray diffraction (XRD) patterns and digital photographs of the

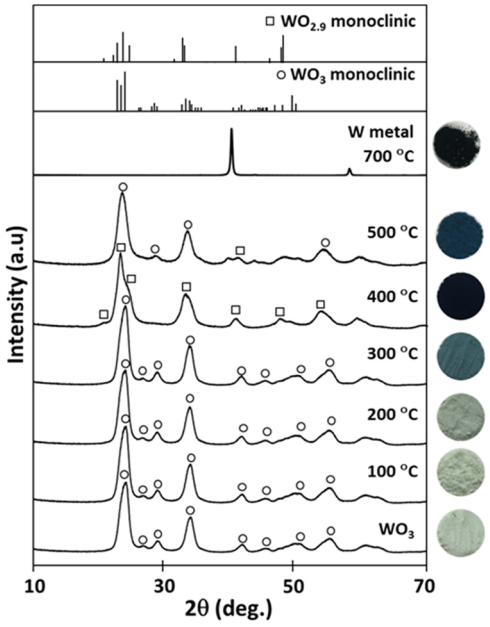

Figure 1. XRD patterns and digital photographs of the WO_3 NPs and WO_x NPs reduced at different temperatures for 1 h under a H_2 gas atmosphere.

plasma-synthesized WO_3 NPs and WO_x NPs synthesized under reduction temperatures ranging from 100 to 700 °C for 1 h. The XRD pattern of the pale green WO_3 NPs could be assigned to the monoclinic crystal structure based on PDF no. 43-1035. The main diffraction peaks at 2θ = 24.2, 26.7, and 34.0° corresponded to the ⟨020⟩, ⟨200⟩, and ⟨202⟩ planes, respectively. Similar XRD patterns were observed for the WO_x NPs reduced at 100−300 °C. However, the color of the WO_x NPs gradually changed from green to bluish green to teal blue. The change in color was caused by oxygen loss within the crystal structure, which led to a change in the W valence state. During reduction, some of the initial W^{6+} were reduced to W^{5+} and W^{4+}, which were responsible for the color change of the NPs.[5,22−24]

$WO_{2.9}$ NPs with a navy-blue color were obtained when the WO_3 NPs were reduced at 400 °C. The XRD pattern was consistent with PDF no. 05-0386 of the monoclinic $WO_{2.9}$ crystal structure. As discussed above, the darkening of the WO_x NP color was associated with an increase in the amount of oxygen deficiencies. More oxygen vacancies within the crystal structure resulted in darker particles. When the reduction temperature was increased to 500 °C, the dominant phase of the WO_x NPs was WO_3 monoclinic crystal structure. A weak peak of $WO_{2.9}$ monoclinic crystal structure was still observed, as well as new broad peaks at 2θ of 40−55°. The color of the WO_x (500 °C) NPs was peacock blue violet. The broad peaks could be assigned to a set of complex structures of different phases of WO_x NPs that were hard to distinguish. WO_3 monoclinic peaks were observed because the NPs had a very active surface, which rapidly oxidized when exposed to the atmosphere. When reduced at 700 °C, NPs with a black color were obtained. The XRD pattern showed that the WO_x (700 °C) NPs were pure W metal, and that the WO_3 NPs had been over reduced.

Figure 2 shows transmission electron microscopy (TEM) images of the WO_3 NPs and WO_x NPs synthesized under different reduction temperatures for 1 h. Figure 2a shows the pristine WO_3 NPs, which had an average diameter (d_p) of 6 nm. Increasing the reduction temperature from 100 to 500 °C yielded monodisperse WO_x NPs with d_p values of 7−11 nm, respectively, as shown in Figure 2b−f. Figure 2g shows a TEM image of the sample prepared at 700 °C, in which the NPs were sintered with a d_p of approximately 20 nm.

WO_3 NPs reportedly readily sinter at annealing temperatures higher than 300 °C.[25] It was reported that when pure WO_3 was reduced without hydrogen, the agglomeration of small tungsten crystals occurred. However, during the reduction of WO_3 to WO_x in the current study, the crystal transformation of WO_x occurred simultaneously with the depletion of oxygen from the surface layer. Oxygen vacancies readily formed during the reduction of tungsten oxide under the hydrogen atmosphere because the chemical potential of oxygen decreases significantly at high temperature and low oxygen partial pressure.[11] As a result, the size and shape of the original WO_3 NPs were maintained in the WO_x NPs. Specific surface areas (S_{BET}) of the NPs were calculated to further investigate the effect of reduction temperature on sintering. S_{BET} values are shown in Figure 2h. The S_{BET} of the WO_x NPs was not significantly affected by reduction at temperatures up to 500 °C. However, the S_{BET} of the WO_x (700 °C) NPs was lower than the others, further suggesting that the NPs sintered during heat treatment at 700 °C.

The above results suggested that the reduction of WO_3 was a very sensitive process. WO_3 NPs were reduced to W metal at a relatively low temperature (700 °C) and short reduction time (1 h). According to a previous study, the phase transformation pathway is: $WO_3 \rightarrow WO_{2.9} \rightarrow WO_{2.7} \rightarrow W$.[26,27] However, the exact reduction temperature and time required to obtain these phases depend on the synthesis method. In the current study, the reduction temperature played an important role in producing WO_x NPs. Though the change in crystal structure was not readily apparent from the XRD patterns, differing amounts of oxygen vacancies within the WO_x structure were apparent from the different colors of the NPs.

To further investigate the effect of the reduction temperature on the WO_x crystal structure, the reduction temperature was varied over a narrower range of 400−475 °C. XRD patterns of WO_x NPs synthesized under these reduction temperatures are shown in Figure 3. A slight increase in reduction temperature changed the crystal structure of the WO_x NPs. As discussed above, the crystal structure of the intermediate Magnéli phase $WO_{2.9}$ was observed following reduction at 400 °C. NPs with a mixed $WO_{2.0}$ (PDF no. 48-1827) and $WO_{2.7}$ (PDF no. 36-101) structure were obtained

DOI: 10.1021/acsomega.8b01110
ACS Omega 2018, 3, 8963−8970

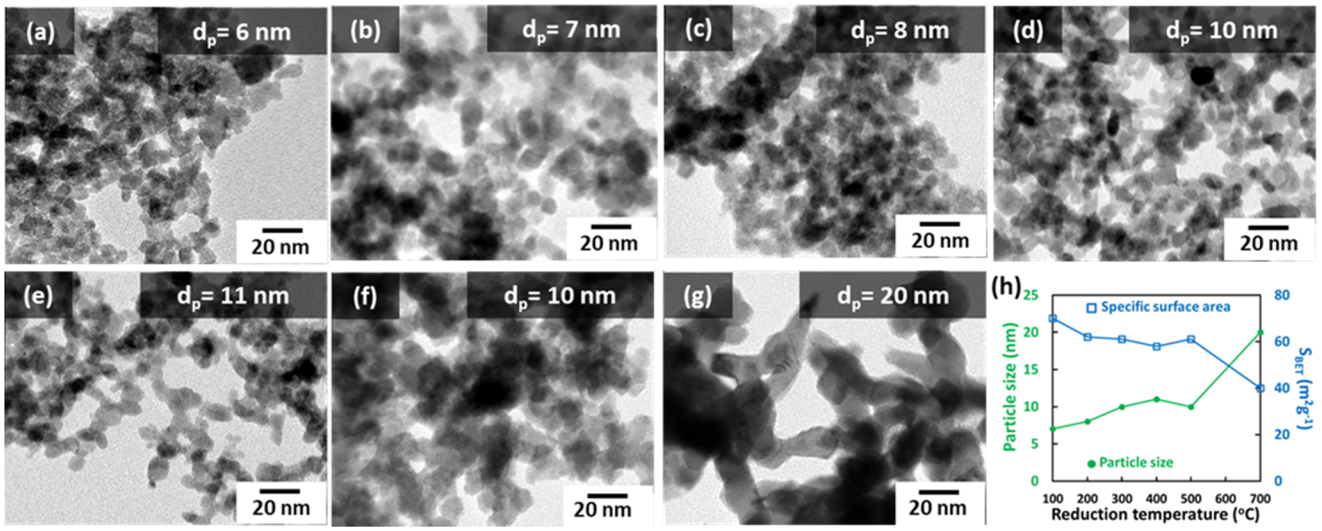

Figure 2. TEM images of the (a) WO_3 NPs and WO_x NPs reduced at (b) 100 °C, (c) 200 °C, (d) 300 °C, (e) 400 °C, (f) 500 °C, and (g) 700 °C. (h) Summary of the effect of reduction temperature on particle size and specific surface area (S_{BET}) of the WO_x NPs. The particle size and S_{BET} of the WO_3 NPs were 6 nm and 71 m^2 g^{-1}, respectively. The average particle diameters (d_p) were derived from topological measurements of more than 300 particles.

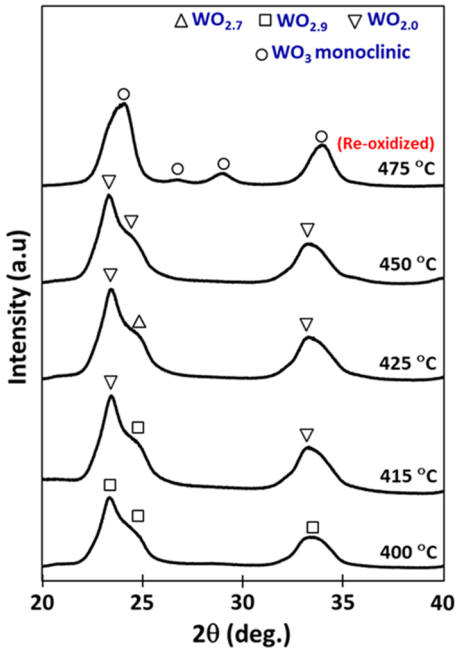

Figure 3. XRD patterns of WO_x NPs reduced at 400−475 °C for 1 h under a H_2 gas atmosphere.

following reduction at 425 °C. The $WO_{2.0}$ phase was obtained following reduction at 450 °C.

After reduction at 475 °C, the surface of the WO_x NPs reoxidized when exposed to open air. This was evidenced by the XRD pattern of the resulting NPs corresponding to the WO_3 monoclinic crystal structure. This occurred because at this temperature the reduction proceeded deeper into the bulk of the NPs, compared with reduction at lower temperature. The high amount of oxygen vacancies and free electrons made the NPs highly unstable and reactive to open air. TEM images of WO_x NPs synthesized at 400−475 °C are shown in Figure S1 (see Supporting Information). The d_p values of these NPs were approximately 10−11 nm. This confirmed that the reduction temperature affected the crystal structure more than the particle morphology and size.

$WO_{2.7}$ is the most stable phase of WO_x for many applications.[11] However, it is difficult to obtain NPs of pure $WO_{2.7}$ phase because the conversion from WO_3 to $WO_{2.0}$ is an extremely rapid reaction. In published studies, identification of the $WO_{2.7}$ phase was carried out solely by observations of color.[2,28]

To understand better about the crystal structure of the as-synthesized WO_x NPs, a high-resolution TEM (HR-TEM) imaging analysis was carried out for several samples, and the obtained images are shown in Figure 4. Figure 4a,b, which, respectively, shows a lattice spacing of 3.92 Å for the WO_x (300 °C) NPs and 3.91 Å for the WO_x (400 °C) NPs, confirms that WO_3 monoclinic crystal structure is still the dominant phase inside the nanoparticles. However, WO_x NPs reduced at 425 °C (Figure 4c) were observed to have a narrower lattice spacing of around 3.59 Å and several displacements (marked by the green rectangle in the picture), which confirmed the presence of WO_x crystal structure as modeled in a previous study.[29] When the WO_3 NPs were reduced at 500 °C, the obtained crystal structure was irregular compared to the other WO_x NPs. This indicates that the NPs were on their way to form another crystal structure because of the increased amount of oxygen deficiencies compared to when reduced at lower temperatures. However, it was not perfectly structured for a reduction time of 1 h. This irregular structure might also be one of the causes for the highly reactive behavior of the WO_x (500 °C) NPs when exposed to open air.

The behavior of the W−O bonding under different reduction temperatures was investigated by Raman spectroscopy, as shown in Figure S2. The results were in good agreement with the XRD results (Figure 1), in which the WO_3 NPs and WO_x (300 °C) NPs had similar crystal structures from the XRD patterns, but differed visually by their color. Furthermore, they also confirmed that the number of oxygen deficiencies increased as the reduction temperature increased. Detailed analysis of the Raman spectroscopy results is available in the Supporting Information S2.

DOI: 10.1021/acsomega.8b01110
ACS Omega 2018, 3, 8963−8970

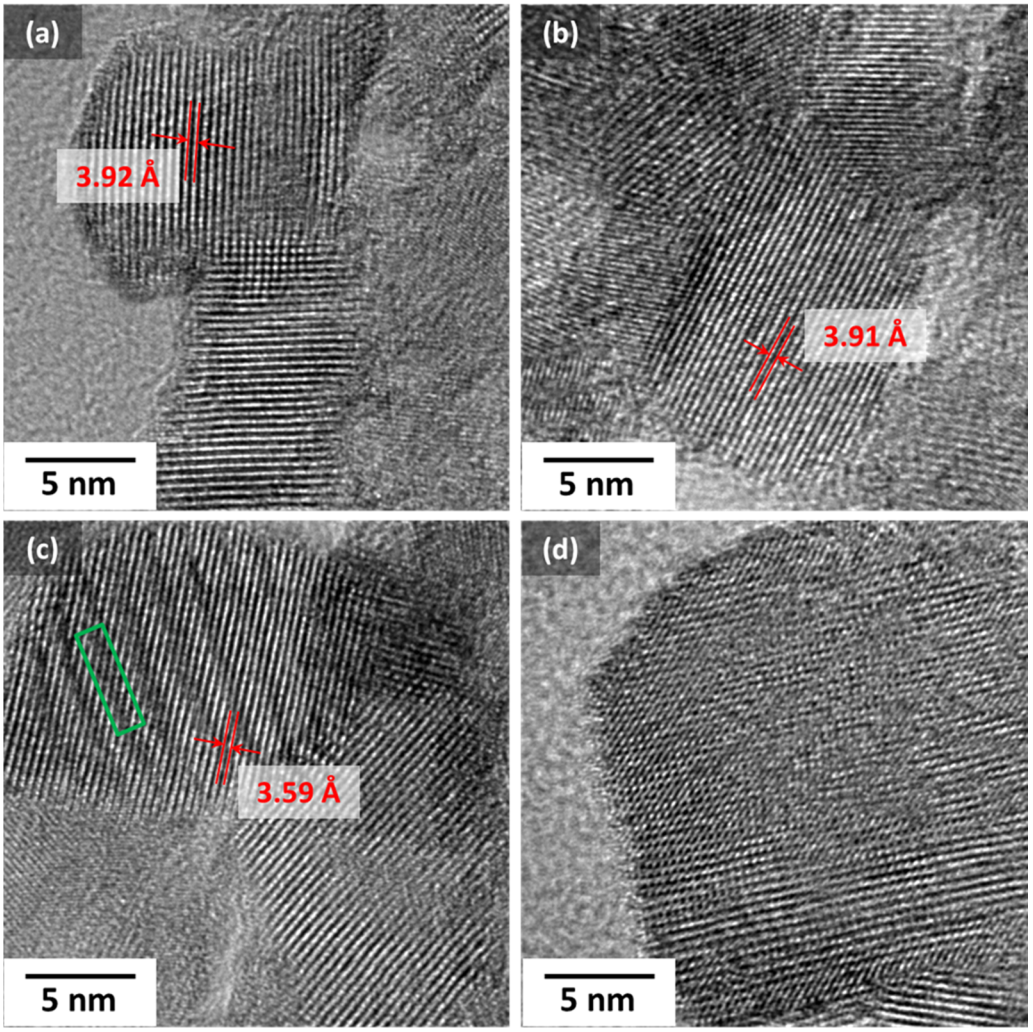

Figure 4. High-resolution TEM (HR-TEM) images for WO_x NPs reduced at (a) 300 °C, (b) 400 °C, (c) 425 °C, and (d) 500 °C.

To investigate further the presence of oxygen deficiencies inside the NP crystal structure, X-ray photoelectron spectroscopy (XPS) measurements were carried out for binding energies around O 1s orbital, and the results are shown in Figure S3 (Supporting Information). The peak intensity of W−O bonding for WO_x (300 °C) was only 32.3% (relative to the total area for three peaks), which is pretty small concerning the fact that the XRD result for this sample showed a dominant WO_3 phase. This indicates the presence of oxygen deficiencies inside their structure. The intensity of the W−O bonding peak became smaller for NPs reduced at 400 and 425 °C, which indicates that more oxygen deficiencies are present inside their structure. However, the peak intensity for the W−O bonding increased significantly for the WO_x (500 °C) NPs, confirming that the particle surface was reoxidized back to WO_3 when exposed to ambient air.

Diffuse reflectance measurements were carried out for the WO_3 NPs and WO_x NPs reduced at 300, 400, 425, 500, and 700 °C, and the results are shown in Figure S6a. From each spectrum, a Tauc plot was derived using the Kubelka−Munk correlation to calculate the band gap.[30] The Tauc plot results are shown in Figure S6b, and the calculated band gaps are summarized in Table 1. A detailed explanation of the method to estimate the band gap value from the diffuse reflectance spectrum is available in the Supporting Information S4.

Table 1. Calculated Band Gaps of the WO_3 NPs and WO_x NPs Reduced at Different Temperatures

sample	band gap (eV)
WO_3	2.61
WO_x (300 °C)	2.62
WO_x (400 °C)	2.58
WO_x (425 °C)	2.37
WO_x (500 °C)	2.51
WO_x (700 °C)	none[a]

[a]The WO_x (700 °C) NPs had no band gap because of their complete reduction to W metal.

Table 1 shows that the reduction process did not significantly change the band gap, except when the NPs were reduced at 425 °C. The WO_x (300 °C) NPs had a band gap similar to that of the initial WO_3 NPs. The band gap of the WO_x (400 °C) NPs was slightly lower, and the value became much narrower when the reduction temperature was 425 °C. This indicates that the band gap became narrower due to the presence of free electrons in the d orbitals of the reduced ions (W^{5+} or W^{4+}), which formed a band tail from the bottom of the conduction band. In the case of the WO_x (700 °C) NPs, no band gap existed because the NPs were completely reduced to W metal, whereas the band gap value of the WO_x (500 °C)

DOI: 10.1021/acsomega.8b01110
ACS Omega 2018, 3, 8963−8970

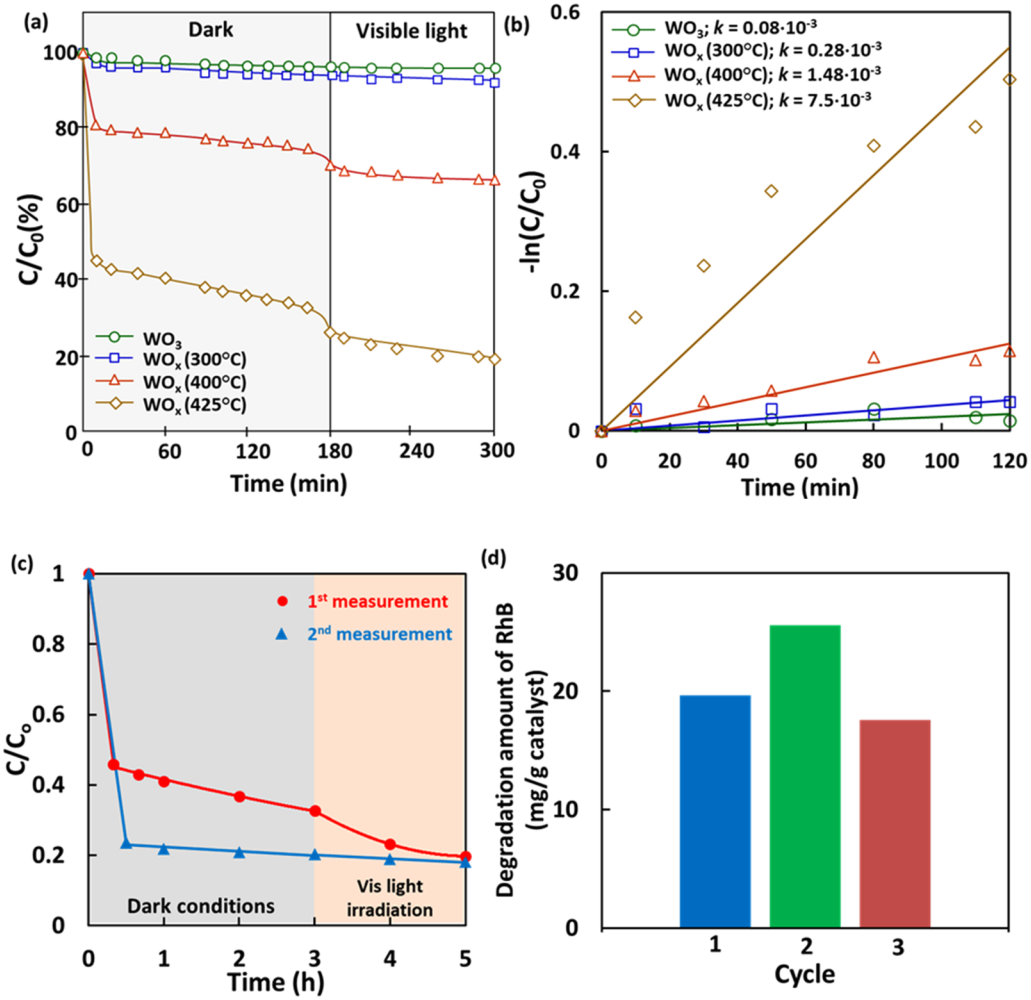

Figure 5. (a) Degradation profiles of RhB over the WO_3 NPs and WO_x NPs reduced at different temperatures, in dark conditions and under visible light irradiation. (b) Corresponding $-\ln(C/C_0)$ versus irradiation time plots for measurements under visible light irradiation. (c) Repeatability check for WO_x (425 °C) NPs. Both measurements were carried out with a time gap of 12 months. (d) Amount of RhB loss per catalyst weight over three cycles of measurement. For each measurement, initial concentration of RhB was 12 mg L^{-1} and observation was carried out in dark conditions (3 h) and under visible light irradiation (2 h).

NPs was bigger than that of the one reduced at 425 °C because their surface was oxidized back to WO_3 as observed before.

Degradation of RhB. Figure 5 shows the degradation of RhB solution with an initial concentration of 12 mg L^{-1} as a function of time over the WO_3 NPs and WO_x NPs reduced at different temperatures. The degradation process of RhB, which includes adsorption and photocatalysis processes, is shown in Figure 5a. Figure 5b shows a plot of their corresponding $-\ln(C/C_0)$ values against the visible light irradiation time. C and C_0 represent the concentration of RhB solution at any given time and its initial concentration, respectively.

Figure 5a shows that the adsorption−desorption equilibriums of RhB in dark conditions over the WO_3 NP and WO_x (300 °C) NP surfaces occurred after approximately 10 min. The RhB concentration after measurement for 3 h in dark conditions and 2 h under visible light irradiation over the WO_x (300 °C) NPs decreased only slightly from that over the WO_3 NPs. The corresponding RhB concentrations were 93 and 96%. The rate constant (k) for the photodecomposition of RhB under visible light irradiation by each sample was evaluated using simplified Langmuir−Hinshelwood kinetics,[30] and the results are shown in Figure 5b. The k values for the WO_3 NPs and WO_x (300 °C) NPs were 0.08×10^{-3} and 0.28×10^{-3} min^{-1}, respectively. These results were in good agreement with the XRD, Raman spectroscopy, and band gap evaluation results, which showed no significant change in the crystal structure and absorption properties when the WO_3 NPs were reduced at 300 °C.

The WO_x (400 °C) NPs showed higher adsorption and photocatalytic performance, with remaining RhB concentrations of 74 and 66% after measurement in dark conditions for 3 h and under visible light irradiation for 2 h, respectively. The k value for this sample was 1.48×10^{-3} min^{-1}. The degradation of RhB increased significantly when the WO_x NPs were reduced at 425 °C. The remaining RhB concentrations for these NPs were approximately 30 and 19% after measurements in dark conditions and under visible light irradiation, respectively, and the k value was 7.5×10^{-3} min^{-1}. This k value was 93 times higher than that for the WO_3 NPs.

The above results indicated that the amount of RhB adsorbed on the particle surface increased as the reduction temperature increased. The adsorption process reached equilibrium after several minutes, which indicated the formation of a monolayer of adsorbed molecules on the

DOI: 10.1021/acsomega.8b01110
ACS Omega 2018, 3, 8963−8970

particle surface.[20] The adsorption ability of the WO_x NPs can be evaluated using the following equations[31]

$$\gamma = (1 - C/C_0) \times 100\% \quad (1)$$

$$Q_c = \gamma C_0 V/m \quad (2)$$

where γ is the adsorption percentage relative to the initial concentration, C_0 is the initial RhB concentration, C is the final RhB concentration after adsorption, V is the volume of RhB solution (L), m is the mass of the WO_x NPs (g), and Q_c is the amount of adsorbed RhB. A summary of the calculation results is shown in Table 2. All measurements were carried out inside a waste model solution of RhB,[32] with an initial concentration at 12 mg L^{-1}. The highest Q_c among the four samples (WO_x NPs reduced at 500 °C are excluded) was 16.16 mg g^{-1} for the WO_x (425 °C) NPs, whereas the lowest Q_c was 0.75 mg g^{-1} for the WO_x (300 °C) NPs. The amount of adsorbed RhB on the surface of the WO_x (425 °C) NPs was 14 times higher than that on the surface of the WO_3 NPs. A repeatability analysis for a time gap of 12 months and a recyclability analysis for three cycles were carried out for the WO_x (425 °C) NPs, and the results are summarized in Figure 5c,d. The WO_x NPs reduced at 425 °C were able to maintain their performance for 1 year and to retain about 90% of their initial performance in the third cycle, indicating a pretty good particle stability. The different adsorption profiles of the WO_x NPs after one year (Figure 5c) might be due to a partially oxidized surface that led to different stabilities and amount of oxygen vacancies inside the NPs.

Table 2. RhB Adsorption Percentage (γ) and Amounts of Adsorbed RhB (Q_c) over the WO_3 NPs and WO_x NPs Reduced at Different Temperatures

sample	γ (%)	Q_c (mg g^{-1})
WO_3	4.96	1.19
WO_x (300 °C)	3.13	0.75
WO_x (400 °C)	25.34	6.08
WO_x (425 °C)	67.34	16.16

Figure 2g shows that the S_{BET} values of the WO_x NPs were smaller than that of the WO_3 NPs. Therefore, the significant increase in adsorption was not attributable to the S_{BET}. Instead, the higher adsorption showed that the WO_x NPs had a greater number of surface active sites than the WO_3 NPs. The surface charge of WO_3 NPs at pH 7 was negative (about −60.1 mV), and they could retain their negative surface charge after being reduced to WO_x NPs (about −49.7 mV for NPs reduced at 425 °C). The interaction between the surface of the WO_3 NPs and cationic RhB was driven by electrostatic attraction. The oxygen vacancies within the crystal structure of the WO_x NPs stimulated electron discharge to the NP surface, which enhanced the RhB−WO_x attraction. Therefore, the WO_x NPs have good potential as an adsorbent for cationic dyes. The presence of free electrons inside the structure of the WO_x NPs allows them to begin degrading RhB prior to visible light irradiation.

In photocatalysis, the band gap plays a crucial role in the absorption of visible light. The WO_x NPs had narrower band gaps than the WO_3 NPs, so exhibited better photocatalytic performance. The presence of oxygen vacancies created a band tail from the initial conduction band.[33] As a result, the lifetime of electron−hole separation was longer, which induced more excited electrons (e^-) to be generated according to[15]

$$WO_x + \text{visible light} \rightarrow WO_x(e^- + h^+) \quad (3)$$

$$W^{6+} + e^- \rightarrow W^{5+} \text{ or } W^{6+} + 2e^- \rightarrow W^{4+} \quad (4)$$

$$W^{5+} + e^- \rightarrow W^{4+} \quad (5)$$

$$W^{4+} + O_2 \rightarrow O_2^{\cdot -} + W^{5+} \quad (6)$$

After photoexcitation, the photocatalytic reaction occurred. In general, the formation of superoxide anions ($O_2^{\bullet -}$) was induced by the reduction of O_2 by electrons, whereas hydroxyl radicals ($OH^\bullet$) were generated from the reaction between H_2O and unstable $O_2^{\bullet -}$.[34] In the final step, $OH^\bullet$ as the dominant active species decomposed the RhB (see Figures S7 and S8 in the Supporting Information). A detailed mechanism of the photocatalytic process was proposed in our previous research.[35] Unfortunately, the edge of the WO_x conduction band was higher than the energy of the H_2/H_2O reaction, and the presence of different oxidation states resulted in rapid electron transport. This meant that the electron−hole pairs tended to recombine rapidly.[36] This was evident from the results where the decomposition rates of RhB under visible light irradiation were lower than those in dark conditions.

Compared with the adsorption process, the photocatalytic performance of the current WO_x NPs requires improvement. Nevertheless, the results provide new information and possibilities for creating adsorbents or catalysts, which can be activated with or without visible light and without using any expensive cocatalyst material, such as Ag and Pt.

CONCLUSIONS

Tungsten blue oxide (WO_x) NPs were prepared via the reduction method under a hydrogen gas atmosphere. The presence of oxygen vacancies in the WO_x NPs could be controlled by varying the reduction temperature. XRD indicated that the crystal structure of the WO_x NPs did not significantly change when they were reduced at temperatures lower than 400 °C, despite their change in color. XRD peaks corresponding to the $WO_{2.9}$, $WO_{2.7}$, and $WO_{2.0}$ phases were observed when the NPs were reduced at 400−500 °C. The optimum reduction temperature was considered to be 425 °C, as evidenced by the presence of $WO_{2.0}$ peaks in the XRD pattern of the resulting WO_x NPs. The band gap of the WO_3 NPs (2.61 eV) decreased to 2.37 eV for the WO_x (425 °C) NPs. Oxygen vacancies played an important role in surface active sites. This resulted in the RhB adsorption of the WO_x NPs being higher than that of the WO_3 NPs. The WO_x (425 °C) NPs decomposed RhB, with up to 32% of RhB remaining in dark conditions and 12% of RhB remaining under visible light irradiation. The corresponding reaction rate constant was 7.5×10^{-3} min^{-1}. The ability to adsorb cationic RhB by the WO_x NPs was 93 times higher than that of the WO_3 NPs. Thus, these findings open new possibilities for fabricating adsorbents and catalysts for various applications. Further study of the physical and chemical properties, including the nanostructuration of the WO_x NPs, to improve the photocatalytic performance is ongoing.

EXPERIMENTAL SECTION

Synthesis of WO_x Nanoparticles. WO_x NPs were synthesized from plasma-synthesized WO_3 NPs (used as

DOI: 10.1021/acsomega.8b01110
ACS Omega 2018, 3, 8963−8970

received from Nishin Engineering Inc., Japan without any additional treatment) with an average particle size of 6 nm. Synthesis was carried out via a thermal reduction process inside a 40 cm long electric vacuum furnace with a diameter of 4 cm. In a typical process, 0.5 g of plasma-synthesized WO_3 NPs were loaded into ceramic boats, which were placed in the center of the furnace. Before heating, the furnace chamber was purged several times with high-purity He gas. The reduction temperature was varied from 100 to 700 °C, with a heating rate of 10 °C min^{-1}, and reduction was carried out for 1 h. Throughout the entire process, high-purity H_2 gas was flown into the furnace chamber at a rate 1 L min^{-1}.

Characterization of Physicochemical Properties. The phase compositions of the particles were identified by X-ray diffraction (XRD) using a Bruker D2 Phaser diffractometer, equipped with Cu Kα radiation and a LinxEye detector. XRD patterns were collected for $10° < 2\theta < 70°$. The morphologies of the particles were investigated using transmission electron microscopy (TEM) analysis (JEM-3000F, JEOL, Japan) at an operating voltage of 297 kV. Specific surface areas were calculated from N_2 adsorption isotherms measured at 77.15 K, using the Brunner−Emmett−Teller (BET) method (BELSORP 28SA, Bel Japan). Prior to surface area determination, the powder samples were dried for 2.5 h at 200 °C under a N_2 atmosphere. The composition of chemical bonding was investigated with a Raman spectrophotometer (T64000 coupled with a He−Cd laser and CCD detector, HORIBA-Jobin Yvon, Japan). XPS measurements (ESCA-3400 with Mg Kα as an X-ray source, Shimadzu Corp., Japan) were carried out to observe the binding energies around O 1s orbital. The XPS results were adjusted to C−C binding energy at 285 eV. To estimate the band gaps of the samples, diffuse reflectance measurements were recorded using an ultraviolet−visible (UV−vis) spectrophotometer (UV-3150, Shimadzu Corp., Japan).

Adsorption and Photocatalytic Performance Analysis. The adsorption and photocatalytic performance of the WO_x NPs were evaluated based on the degradation of RhB. A photoreactor system equipped with a solar simulator (PEC-L11, Peccell Technologies Inc., Japan) was used as the visible light source. In a typical degradation experiment, 100 mg of WO_x NPs was dispersed in 200 mL of RhB solution (12 mg L^{-1}; Wako Pure Chemical Industries Ltd., Japan). The adsorption process was monitored under dark conditions for 3 h before starting the photocatalytic activity measurements. The photocatalytic activity was observed for 2 h under visible light irradiation.

During the photocatalytic activity measurements, O_2 gas was fed into the solution at a rate of 0.2 L min^{-1}, to maintain a constant concentration of dissolved oxygen. The reaction mixture was subjected to continuous stirring (400 rpm) at ambient temperature (25 °C). Aliquots (2 mL) of solution were removed at certain times, which were then centrifuged at 15 000 rpm for 5 min. The supernatant was used to observe the change in RhB concentration over time. For this analysis, a UV−vis absorption spectrophotometer (UV-3150, Shimadzu Corp., Japan) was used to obtain the absorption spectra of samples at given times.

To check the stability of this material, a recyclability analysis was conducted using WO_x NPs reduced at 425 °C. As an initial amount, 100 mg of WO_x (425 °C) NPs was dispersed into 200 mL of RhB solution. The analysis was carried out for three cycles. For each cycle, the initial concentration of the RhB solution was maintained at 12 mg L^{-1}, and the remaining RhB concentration was checked after stirring for 3 h in dark conditions and 2 h under visible light irradiation. Between cycles, a washing treatment to remove all RhB molecules from the catalyst surface was done several times using ultrapure water followed by centrifugation at 15 000 rpm for 15 min. After the RhB molecules were completely removed, the NPs were dried inside a vacuum furnace at 130 °C for 2 h.

■ ASSOCIATED CONTENT

Supporting Information

The Supporting Information is available free of charge on the ACS Publications website at DOI: 10.1021/acsomega.8b01110.

TEM images of WO_x NPs reduced at 400−475 °C; Raman spectroscopy analysis; XPS measurement analysis; and detailed explanation on band gap analysis from diffuse reflectance spectra (PDF)

■ AUTHOR INFORMATION

Corresponding Author

*E-mail: ogit@hiroshima-u.ac.jp. Tel: +81-82-424-3675.

ORCID

Aditya Farhan Arif: 0000-0003-4219-4395

Takashi Ogi: 0000-0003-3982-857X

Notes

The authors declare no competing financial interest.

■ ACKNOWLEDGMENTS

This study was supported by JSPS KAKENHI Grant Numbers 26709061 and 16K13642, was partly funded by the Center for Functional Nano Oxide of Hiroshima University, and was sponsored by the Ministry of Education, Culture, Sports, Science, and Technology of Japan as a scholarship for F.G.R.

■ REFERENCES

(1) Cong, S.; Geng, F.; Zhao, Z. Tungsten oxide materials for optoelectronic applications. *Adv. Mater.* **2016**, *28*, 10518−10528.

(2) Qamar, M.; Fawakhiry, M.; Azad, A.-M.; Ahmed, M.; Khan, A.; Saleh, T. Selective photocatalytic oxidation of aromatic alcohols into aldehydes by tungsten blue oxide (TBO) anchored with Pt nanoparticles. *RSC Adv.* **2016**, *6*, 71108−71116.

(3) Lee, T.; Lee, Y.; Jang, W.; Soon, A. Understanding the advantage of hexagonal WO_3 as an efficient photoanode for solar water splitting: a first-principles perspective. *J. Mater. Chem. A* **2016**, *4*, 11498−11506.

(4) Enferadi-Kerenkan, A.; Do, T.-O.; Kaliaguine, S. Heterogeneous catalysis by tungsten-based heteropoly compounds. *Catal. Sci. Technol.* **2018**, *8*, 2257−2284.

(5) Huang, Z. F.; Song, J.; Pan, L.; Zhang, X.; Wang, L.; Zou, J. J. Tungsten oxides for photocatalysis, electrochemistry, and phototherapy. *Adv. Mater.* **2015**, *27*, 5309−5327.

(6) Tong, H.; Ouyang, S.; Bi, Y.; Umezawa, N.; Oshikiri, M.; Ye, J. Nano-photocatalytic materials: possibilities and challenges. *Adv. Mater.* **2012**, *24*, 229−251.

(7) Li, W.; Xia, F.; Qu, J.; Li, P.; Chen, D.; Chen, Z.; Yu, Y.; Lu, Y.; Caruso, R. A.; Song, W. Versatile inorganic-organic hybrid WO_x-ethylenediamine nanowires: Synthesis, mechanism and application in heavy metal ion adsorption and catalysis. *Nano Res.* **2014**, *7*, 903−916.

(8) Luo, J. Y.; Lin, Y. R.; Liang, B. W.; Li, Y. D.; Mo, X. W.; Zeng, Q. G. Controllable dye adsorption behavior on amorphous tungsten oxide nanosheet surfaces. *RSC Adv.* **2015**, *5*, 100898−100904.

DOI: 10.1021/acsomega.8b01110
ACS Omega 2018, 3, 8963−8970

(9) Jeon, S.; Yong, K. Morphology-controlled synthesis of highly adsorptive tungsten oxide nanostructures and their application to water treatment. *J. Mater. Chem.* **2010**, *20*, 10146−10151.
(10) Ogi, T.; Nandiyanto, A. B. D.; Okuyama, K. Nanostructuring strategies in functional fine-particle synthesis towards resource and energy saving applications. *Adv. Powder Technol.* **2014**, *25*, 3−17.
(11) Song, J.; Huang, Z.-F.; Pan, L.; Zou, J.-J.; Zhang, X.; Wang, L. Oxygen-deficient tungsten oxide as versatile and efficient hydrogenation catalyst. *ACS Catal.* **2015**, *5*, 6594−6599.
(12) Ghosh, S.; Saha, M.; Paul, S.; De, S. Maximizing the photo catalytic and photo response properties of multimodal plasmonic Ag/WO_{3-x} heterostructure nanorods by variation of the Ag size. *Nanoscale* **2015**, *7*, 18284−18298.
(13) Arif, A. F.; Balgis, R.; Ogi, T.; Iskandar, F.; Kinoshita, A.; Nakamura, K.; Okuyama, K. Highly conductive nano-sized Magnéli phases titanium oxide (TiO_x). *Sci. Rep.* **2017**, *7*, No. 3646.
(14) Rinaldi, F. G.; Arif, A. F.; Ogi, T.; Okuyama, K.; Tanabe, E. Strong metal-support interactions (SMSIs) between Pt and Ti^{3+} on Pt/TiO_x nanoparticles for enhanced degradation of organic pollutant. *Adv. Powder Technol.* **2017**, *28*, 2987−2995.
(15) Shen, Z.; Zhao, Z.; Qian, J.; Peng, Z.; Fu, X. Synthesis of WO_{3-x} nanomaterials with controlled morphology and composition for highly efficient photocatalysis. *J. Mater. Res.* **2016**, *31*, 1065−1076.
(16) Bhuyan, B.; Paul, B.; Dhar, S. S.; Vadivel, S. Facile hydrothermal synthesis of ultrasmall $W_{18}O_{49}$ nanoparticles and studies of their photocatalytic activity towards degradation of methylene blue. *Mater. Chem. Phys.* **2017**, *188*, 1−7.
(17) Kim, M.; Lee, B. Y.; Ham, H. C.; Han, J.; Nam, S. W.; Lee, H.-s.; Park, J. H.; Choi, S.; Shin, Y. Facile one-pot synthesis of tungsten oxide (WO_{3-x}) nanoparticles using sub and supercritical fluids. *J. Supercrit. Fluids* **2016**, *111*, 8−13.
(18) Lassner, E.; Schubert, W.-D. Tungsten blue oxide. *Int. J. Refract. Met. Hard Mater.* **1995**, *13*, 111−117.
(19) Seifollahi Bazarjani, M.; Hojamberdiev, M.; Morita, K.; Zhu, G.; Cherkashinin, G.; Fasel, C.; Herrmann, T.; Breitzke, H.; Gurlo, A.; Riedel, R. Visible light photocatalysis with c-WO_{3-x}/WO_3 × H_2O nanoheterostructures in situ formed in mesoporous polycarbosilane-siloxane polymer. *J. Am. Chem. Soc.* **2013**, *135*, 4467−4475.
(20) Bu, Y.; Chen, Z.; Sun, C. Highly efficient Z-scheme Ag_3PO_4/Ag/WO_{3-x} photocatalyst for its enhanced photocatalytic performance. *Appl. Catal., B* **2015**, *179*, 363−371.
(21) Liu, C.; Yang, Z.; Li, Y. Preparation and enhanced visible-light photocatalytic activity of Pancake Rocks-like WO_{3-x}/C nanocomposite. *RSC Adv.* **2016**, *6*, 32983−32988.
(22) Chatten, R.; Chadwick, A. V.; Rougier, A.; Lindan, P. J. The oxygen vacancy in crystal phases of WO_3. *J. Phys. Chem. B* **2005**, *109*, 3146−3156.
(23) Migas, D.; Shaposhnikov, V.; Borisenko, V. Tungsten oxides. II. The metallic nature of Magnéli phases. *J. Appl. Phys.* **2010**, *108*, No. 093714.
(24) Uppachai, P.; Harnchana, V.; Pimanpang, S.; Amornkitbamrung, V.; Brown, A. P.; Brydson, R. M. A substoichiometric tungsten oxide catalyst provides a sustainable and efficient counter electrode for dye-sensitized solar cells. *Electrochim. Acta* **2014**, *145*, 27−33.
(25) Purwanto, A.; Widiyandari, H.; Ogi, T.; Okuyama, K. Role of particle size for platinum-loaded tungsten oxide nanoparticles during dye photodegradation under solar-simulated irradiation. *Catal. Commun.* **2011**, *12*, 525−529.
(26) Haboury, R.; Pal, U. B.; Zink, P. A.; Gopalan, S.; Basu, S. N. Study of an energy storage and recovery concept based on the W/WO_3 redox reaction: part I. Kinetic study and modeling of the WO_3 reduction process for energy storage. *Metall. Mater. Trans. B* **2012**, *43*, 1001−1010.
(27) Singla, G.; Singh, K.; Pandey, O. Structural and thermal properties of in-situ reduced WO_3 to W powder. *Powder Technol.* **2013**, *237*, 9−13.
(28) Weil, M.; Schubert, W.-D. *The Beautiful Colours of Tungsten Oxides*; Tungsten Newsletter; International Tungsten Industry Association: London, 2013; pp 1−9.
(29) Bursill, L.; Hyde, B. CS families derived from the ReO_3 structure type: An electron microscope study of reduced WO_3 and related pseudobinary systems. *J. Solid State Chem.* **1972**, *4*, 430−446.
(30) Ohtani, B. Revisiting the fundamental physical chemistry in heterogeneous photocatalysis: its thermodynamics and kinetics. *Phys. Chem. Chem. Phys.* **2014**, *16*, 1788−1797.
(31) Jiang, X.; Huang, J. Adsorption of Rhodamine B on two novel polar-modified post-cross-linked resins: equilibrium and kinetics. *J. Colloid Interface Sci.* **2016**, *467*, 230−238.
(32) Arutanti, O.; Ogi, T.; Nandiyanto, A. B. D.; Iskandar, F.; Okuyama, K. Controllable crystallite and particle sizes of WO_3 particles prepared by a spray-pyrolysis method and their photocatalytic activity. *AIChE J.* **2014**, *60*, 41−49.
(33) Yan, J.; Wang, T.; Wu, G.; Dai, W.; Guan, N.; Li, L.; Gong, J. Tungsten oxide single crystal nanosheets for enhanced multichannel solar light harvesting. *Adv. Mater.* **2015**, *27*, 1580−1586.
(34) Shahmoradi, B.; Maleki, A.; Byrappa, K. Photocatalytic degradation of amaranth and brilliant blue FCF dyes using in situ modified tungsten doped TiO_2 hybrid nanoparticles. *Catal. Sci. Technol.* **2011**, *1*, 1216.
(35) Arutanti, O.; Nandiyanto, A. B. D.; Ogi, T.; Kim, T. O.; Okuyama, K. Influences of porous structurization and Pt addition on the improvement of photocatalytic performance of WO_3 particles. *ACS Appl. Mater. Interfaces* **2015**, *7*, 3009−3017.
(36) Arutanti, O.; Arif, A. F.; Balgis, R.; Ogi, T.; Okuyama, K.; Iskandar, F. Tailored synthesis of macroporous Pt/WO_3 photocatalyst with nanoaggregates via flame assisted spray pyrolysis. *AIChE J.* **2016**, *62*, 3864−3873.

DOI: 10.1021/acsomega.8b01110
ACS Omega 2018, 3, 8963−8970